Supplementary Information

Liquid-Solid Hybrid Power Converter For High Frequency Energy Conversion

Table of contents

Supplementary Tables

Supplementary Movies

References

Supplementary Note 1

To establish the movement model of liquid metal accurately, we also consider the retardation force. When the LMC contacts the bottom substrate of the conductor channel,friction arises, which can influence the movement of the liquid metal and potentially affect the circuit performance[1]. During the process of LMD's movement, there are three kinds of retardation forces. The first one is the viscous friction between the droplet and its surrounding electrolyte. The viscous force on a spherical particle moving through a fluid is given by the Stokes' well-known formula[2;3]:

$$f_1 = 6\pi r\eta v_0 \tag{1}$$

where η is the viscosity of the electrolyte, and v_0 is the current droplet velocity. The second one is the friction between the droplet and the substrate, and its expression is as follows:

$$f_2 = \rho_{\text{diff}}\nu g\beta \tag{2}$$

where ρ_{diff} is the density difference between the droplet and the electrolyte, ν is the volume of the droplet, g is the gravitational acceleration, and β is the friction coefficient between the droplet and the bottom substrate.

The third one is the capillary force which is induced by the deformation of the LMD acting against the movement can be calculated as[4;5],

$$f_3 = 2\gamma r(\cos\theta_{\text{r}} - \cos\theta_\alpha) \tag{3}$$

where θ_{r} and θ_α are the advancing and receding contact angles, respectively. This term accounts for the capillary resistance associated with contact-angle hysteresis when a three-phase contact line is present between the droplet, electrolyte and channel surface.

The acceleration of the droplet, a_{f}, induced by resistance can be expressed as

$$\begin{aligned} a_{\text{f}} &= \frac{f_1 + f_2 + f_3}{m} = \frac{6\pi r\eta v_0 + \rho_{\text{diff}}\nu g\beta + 2\gamma r(\cos\theta_{\text{r}} - \cos\theta_\alpha)}{\frac{4\pi r^3\rho}{3}} \\ &= \frac{9\eta v_0}{2r^2\rho} + \frac{\rho_{\text{diff}} g\beta}{\rho} + \frac{3\gamma(\cos\theta_{\text{r}} - \cos\theta_\alpha)}{2\pi r^2\rho} \end{aligned} \tag{4}$$

So the total acceleration, a,is

$$\begin{aligned} \mathrm{a} &= a_{\mathrm{F}} - a_{\mathrm{f}} \\ &= \frac{9q_0 A_{\mathrm{current}}}{\rho(3A_{\mathrm{current}} r - 2\pi r^3)} \frac{V_{\mathrm{electrode}}}{L} - \frac{9\eta v_0}{2r^2\rho} - \frac{\rho_{\mathrm{diff}} g\beta}{\rho} - \frac{3\gamma(\cos\theta_{\mathrm{r}} - \cos\theta_{\alpha})}{2\pi r^2 \rho} \end{aligned} \tag{5}$$

The cross-sectional area of the current path ($A_{current}$), the density of the liquid metal droplet (ρ), the initial charge (q_0) on the EDL, the total length of the current path (L), the viscosity of the electrolyte (η), the density difference between the droplet and the electrolyte (ρ_{diff}), the gravitational acceleration (g), and the friction coefficient between the droplet and the bottom substrate (β), are all constant. According to equation(5), the movement of the LMC is affected by many factors, such as the radius of the LMC, the concentration of the electrolyte solution and the applied electric field. The movement of the LMC is further illustrated by experiments.

Supplementary Note 2

The skin effect is the frequency-dependent crowding of alternating current (AC) toward the surface of a good conductor[6]. This phenomenon causes AC to predominantly flow near the surface of a solid conductor, reducing the effective cross-sectional area available for the electron flow. As a result, the resistance of the conductor increases for AC, compared to its resistance under direct current (DC) conditions. Skin effect becomes more noticeable as the frequency of the AC increases, leading to a situation where the interior of the conductor contributes little to current conduction, effectively rendering the conductor as if it were hollow.

This characteristic of the skin effect has notable practical implications, especially in high frequency applications. For instance, at Radio Frequency (RF), using hollow metal rods instead of solid metal wires in antennas can achieve weight and cost savings without sacrificing performance. Hollow method leverages the skin effect by acknowledging that the current predominantly travels on the outer surface of the conductor, thus maintaining efficiency in RF energy/signal transmission and reception. As shown in Supplementary Fig. 2.

Additionally, the impact of frequency on the effective resistance of a solid wire conductor is significantly influenced by the wire's gauge. In this context,

larger gauge size exhibit a more pronounced skin effect at a given frequency compared to smaller gauge size. This skin effect, predominantly observed at higher frequencies, leads to a concentration of current near the surface of the conductor, thereby altering its effective resistance. To address this phenomenon, there is an equation designed to approximate the skin effect for frequencies above 1 MHz.

$$R_{\mathrm{AC}} \approx \left(R_{\mathrm{DC}}\, X_g\right) \sqrt{f}, \tag{6}$$

where f is the frequency in MHz and X_g is a gauge-dependent coefficient. Equation (6) captures the characteristic $R_{\mathrm{AC}} \propto \sqrt{f}$ trend due to current crowding. As shown in Supplementary Fig. 4.

For the conductor, the displacement current density $\partial \mathbf{D}/\partial t$ is negligible compared with the conduction current density $\mathbf{J}$, i.e. $|\omega\varepsilon| \ll \gamma$. Accordingly, the skin effect can be analyzed in the magneto-quasi-static (MQS) limit by neglecting the displacement current.

Let there be a conductor (a semi-infinite conductor), which a sinusoidal alternating current i flows in the conductor; and the current density J has only a single y-direction component, then the electric field and the current are in the same direction. When $x \to \infty$, $\tilde{E}_y$ should be a finite value[6;7].

Define $\alpha + j\beta = k = \sqrt{\pi f\, \mu\gamma}\,(1+j)$, the current density is distributed in the conductor as:

$$J_y = \gamma\, E_y = \gamma\, E_0\, e^{-\alpha x} e^{-j\beta x} \tag{2}$$

where γ is the conductivity and μ is the permeability.

From the above equation, the amplitude of the electromagnetic field as well as the current density along the longitudinal x-direction of the conductor are all decayed according to the exponential law $e^{-\alpha x}$, and the phase is also changed accordingly. This indicates that the electromagnetic field and current density are large near the surface of the conductor, and the deeper inside the conductor, the smaller the electromagnetic field and current density.

The penetration depth d is commonly used in engineering to express the degree of skin effect in a conductor. It is equal to the distance travelled when the amplitude of the electromagnetic field decays to its surface value $1/e$, i.e.

$$d = \frac{1}{\alpha} = \frac{1}{\beta} = \frac{1}{\sqrt{\pi f\, \mu\gamma}} \tag{3}$$

This result shows that the higher the frequency and the better the conductor, the more significant the skin effect is. As shown in Supplementary Fig. 5.

Supplementary Note 3

Among the eddy current losses, the most significant losses are the proximity effect and the skin effect. The proximity effect is the redistribution of current in nearby parallel AC conductors due to magnetic effects[8]. This effect causes the current to concentrate on the side farther from a neighboring conductor when the AC currents flow in the same direction, and closer when they flow in opposite directions.

The proximity effect results from eddy currents and electromagnetic induction within the conductor, induced by the time-varying magnetic fields of adjacent conductors. For instance, in a coil with multiple wire turns carrying alternating current, the proximity effect leads to the current being concentrated in areas of each turn that are farther from adjacent wires. This results in a reduced effective cross- sectional area for the current to flow through, consequently increasing the current density and the conductor's AC resistance. As the frequency increases, so does the current density on one side of the conductor, intensifying the proximity effect. The effect intensifies with frequency, leading to increased resistance in neighboring wires carrying the same current at higher frequencies.

The proximity effect can significantly increase the AC resistance of adjacent conductors when compared to its resistance to DC current. At higher frequencies, the AC resistance of a conductor can easily exceed ten times its DC resistance.

Supplementary Note 4

The skin effect and proximity effect phenomenon cause the current to converge on the surface layer of the conductor, which reduces the cross-sectional area of the conductor through which the current flows, leading to an increase in resistance. In the meantime, two effects cause a reduction in current density in the internal region of the coil, which may reduce the inductance of the inductor.

For conductors like cables with insulating materials, high-frequency conditions also produce dielectric losses[9]. Dielectric loss quantifies the electromagnetic energy dissipation inherent in dielectric materials, which are caused by the finite electrical conductivity of the dielectric material, usually associated with the leakage current and voltage in the dielectric. At high

frequencies, the electromagnetic response of the dielectric material results in more substantial energy loss. This is because the rapidly alternating electric field causes the dielectric material's molecules to continuously realign themselves, consuming energy in the process. Consequently, dielectric losses become more pronounced in high-frequency applications, posing a significant challenge in the design and operation of electrical and electronic systems that operate under such conditions.

Assume there is a single-layer copper foil, where 'w' and 'h' represent the width and thickness of the copper foil, respectively; and 'w' is significantly greater than 'h'. Consequently, it is assumed that the direction of the magnetic field strength on both the upper and lower surfaces of the copper foil is parallel to its surface, and the solution for the field strength within the copper foil is a one-dimensional function:

Define $v = h/d$ (d is skin depth). This means expressing the thickness of the conductor in terms of several skin depths, thus allowing the parameter v to simultaneously reflect the impact of the copper conductor's thickness and operating frequency on its power loss.

The losses in one-dimensional windings can be represented as the superposition of skin losses and proximity losses. The losses in one-dimensional conductors, due to the skin effect and proximity effect within the conductor are orthogonal[6;9–11].Define boundary $H_y(x=0) = H_y^{(1)}$, $H_y(x=-h) = H_y^{(2)}$, then

$$H_y(x) = \frac{H_y^{(1)} \sinh[k(h-x)] + H_y^{(2)} \sinh(kx)}{\sinh(kh)} \tag{4}$$

Therefore, the power loss per unit length of the copper foil in the z-axis direction can be expressed as the sum of the following two equations:

$$P_s = \frac{w}{4\gamma d} \left| H_y^{(2)} - H_y^{(1)} \right|^2 \frac{\sinh v + \sin v}{\cosh v - \cos v} \tag{5}$$

$$P_p = \frac{w}{4\gamma d} \left| H_y^{(1)} + H_y^{(2)} \right|^2 \frac{\sinh v - \sin v}{\cosh v + \cos v} \tag{6}$$

Where P_s represents the loss caused by the skin effect, that is, the loss in the conductor caused solely by the current passing through it without any external magnetic field. P_p represents the loss caused by the proximity effect; that is, the loss induced in the conductor by eddy currents due to an external magnetic field, even when there is no net current in the conductor.

Analyzing the expression for skin effect loss in equation (5), under the condition of a certain current in the conductor and a one-dimensional model, according to Ampere's circuital law, the loss caused by the skin effect initially decreases as the thickness of the conductor increases, reaching a minimum when the conductor thickness is equal to π times the skin depth. Afterwards, the conductor loss changes slowly with the thickness and has a limit.

Since the conductor loss is the sum of the skin effect loss and the proximity effect loss, and they both have extreme values with respect to the conductor thickness, the total loss of the conductor also has an extreme value with respect to the conductor thickness.

When the conductor structure and its current are fixed, losses due to skin and proximity effects tend to increase with rising frequency.

When plots the trend of losses due to skin effect and proximity effect with frequency, the conductor thickness $h = 0.2\,\mathrm{mm}$, where $\gamma = 5.8 \times 10^7\,\mathrm{S/m}$ and $\mu = 4 \times \pi \times 10^{-7}\,\mathrm{H/m}$. When the conductor thickness takes different values, the results are consistent with the trend.

The current density distribution in the circular and the square wires during the full load working of the transformer are illustrated. As the Supplementary Fig. 5. shows, the current density is very low for center parts of the wires, but the current density is much higher for the parts near the surface.

To further test the impact of higher frequencies on the skin effect and proximity effect, it demonstrates the current density in the transformer's windings at a frequency of 20 kHz. It reveals a deeper penetration of current within the wires compared to the conditions where the frequency was 20 MHz. This comparison clearly indicates how the skin effect varies with frequency, affecting the depth of current penetration.

At 20 kHz, the peak current density within conductors is significantly lower than at 20 MHz, exhibiting a more uniform distribution. Notably, the skin-effect manifests less intensely.

Supplementary Note 5

Most of the circuit topologies in the energy conversion domain operate at frequencies near or below 100 kHz. At the low end, conventional rectifiers and intermediate-frequency transformers typically operate in the 50-60 Hz range and are widely used in grid-level systems. Topologies such as buck, boost, and push-pull converters generally function within the 70-500 kHz range and are

moderately prevalent. More advanced and widely adopted configurations including LLC resonant converters, dual active bridges, phase-shift full-bridge converters, and zero-voltage/zero-current switching topologies commonly operate between 100 and 500 kHz. Given this distribution, Galinstan LMC, which maintain favorable electrical performance across this frequency range, are well suited for deployment in liquid-solid power electronics.

To evaluate the AC behavior of the LMC as it is essential for LMC performs to be reliable under AC conditions.The conductor was connected in series with a 1 Ω resistor and an AC voltage source to form a circuit loop. An oscilloscope was used to measure the voltage across a section of the conductor. The input voltage was fixed at 20 V, while the frequency was swept across six gears, 10 Hz, 100 Hz, 1 kHz, 10 kHz, 100 kHz, and 1 MHz. Observing the voltage drop across the conductor at each frequency, the variation in conductor loss under different high-frequency conditions was quantified. As shown in Supplementary Fig. 7.

Experimental results revealed that the Galinstan conductor exhibited measurable signal loss beginning at 100 kHz, and significant loss observed at 1 MHz. At lower frequencies, the voltage drop across these conductors remained negligible. For comparison, a copper conductor of similar length and cross-sectional radius was tested under the same conditions. At 100 kHz, two types of conductors exhibited comparable voltage drops. Meanwhile, at 1 MHz, the copper conductor showed a partial voltage drop of approximately 40 mV, while the Galinstan conductor showed drops of around 60 mV. These results indicate that while copper exhibits slightly lower loss at higher frequencies, the difference is very minor when operating for power converters.

Supplementary Note 6

To minimize experimental variability, we designed a series of comparative experiments based on equation (5) to systematically examine the effects of NaOH concentration, applied voltage, channel length, channel width, and actuation cycles on LMC movement, without accounting for the influence of contact angle.

At the onset of LMD movement, the initial LMC velocity satisfies $v_0 = 0$, and the total acceleration satisfies $a \geq 0$. Under constant experimental conditions–including equipment configuration and electrolyte concentration–the parameters A_{current}, q_0, r, L, Z, r_{diff}, g, and b can be considered invariant

throughout the movement.

Firstly, the concentration of NaOH influences the velocity of Galinstan. In this section, we conducted grouped experiments with concentrations ranging from 0.2 mol/L to 0.8 mol/L, employing a 0.1 mol/L gradient. The image shows the position of the entire Galinstan within the channel one second after movement began. As shown in Supplementary Fig. 8.

The results showed that a 0.5 mol/L NaOH solution allowed relatively fast movement of liquid metal with fixed dimensions in the 5 mm-wide channel used in this study.

Next, we compared the effects of different voltage levels applied to both graphite electrodes. A DC power supply was used to apply voltages of 9, 10, 12, 14, 15, 18, 20, 22, 25, and 30 V in separate experiments. The position of the LMC was recorded one second after the onset of movement for each voltage level. As shown in Supplementary Fig. 9.

The results indicate that the voltage has a negligible effect on the movement speed of the LMC at or below 18 V, begins to exert a noticeable influence between 18 V and 25 V, and shows a diminishing impact at voltages above 25 V.

The third experiment examined the effect of channel length, defined as the distance between the graphite electrodes, on LMC movement. In this setup, five channels with different lengths were simultaneously tested by connecting their respective positive and negative electrodes to a common 15 V power source, ensuring identical voltage across all channels. The five channels used in this experiment had lengths of 38.5 mm, 58.5 mm, 78.5 mm, 88.5 mm, and 98.5 mm, respectively. The image captures the state of the LMCs 0.25 s after voltage application. As shown in Supplementary Fig. 10.

Experimental results show that channel length specifically the distance between graphite electrodes has a negligible effect on LMC movement. After equal durations of operation, the LMC exhibited nearly identical travel distances, with minor deviations likely arising from resistance associated with the movement of the LMC and fluid interactions within the channel.

The fourth experiment investigated the influence of channel width, corresponding to the diameter of the LMC, on its movement. Five channel groups were used, each with a fixed length of 58.5 mm, but with widths of 3 ± 0.5 mm, 4 ± 0.5 mm, 5 ± 0.5 mm, 6 ± 0.5 mm, and 7 ± 0.5 mm. The experimental results diagram shows the LMC positions 0.9 s after the initiation of movement. As shown in Supplementary Fig. 11

Experimental results suggest that the channel width, equivalent to the

LMC diameter, should not be too small, as narrow channels impede LMC movement due to increased friction and confinement effects. Conversely, excessively large diameters may reduce propulsion efficiency or introduce instability in movement.

The fifth experiment was a cycle count test aimed at evaluating whether repeated actuation affects LMC speed. To assess long-term performance for potential use in periodic converters, the LMC's initial movement state was compared with its behavior after 200 reciprocating cycles. The experimental image presents the LMC position recorded 0.16 s after the onset of movement. As shown in Supplementary Fig. 12.

Experimental results show that the LMC maintains consistent movement characteristics after 200 actuation cycles, with no observable degradation in performance. This suggests that the LMC can undergo repeated operation without affecting the overall conversion speed of the LHPC system. For high-frequency operation, the LM and NaOH solutions can be rapidly recovered and redeployed to enable continuous use.

Based on the results of the comparative experiments, most channels in the subsequent tests were redesigned with a width of 5 mm and a height of 7 mm to optimize LMC performance.

Supplementary Figures

Supplementary Fig. 1 — Applications across energy mobility and electronics. (Elements in Fig. 1a created with freepik.com, released under a license. Source data are provided as a Source Data file.)

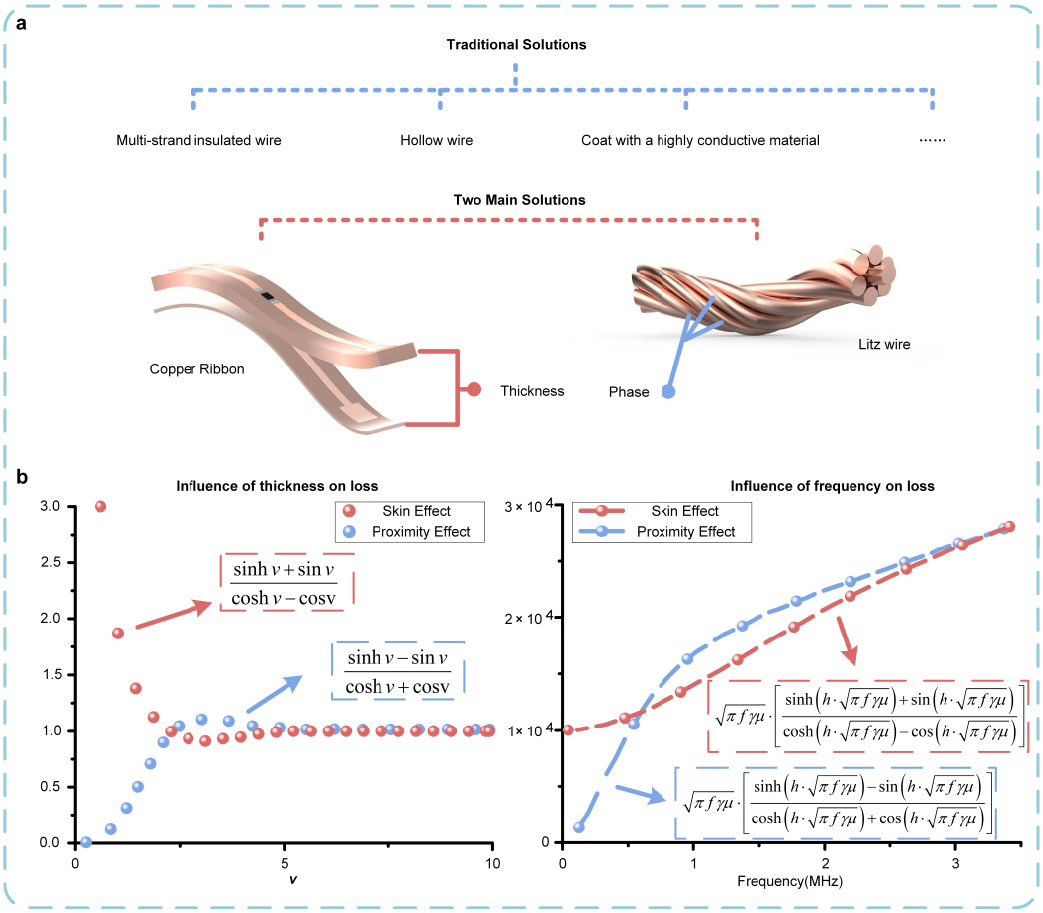

Supplementary Fig. 2 — Several traditional solutions[7;11–15]. Two main solutions–reduced thickness and Litz wire.

Supplementary Fig. 3 — Ultramicroscopic photograph of Galinstan. Ultramicroscopic images of Galinstan before and after immersion in NaOH solution. In air, Galinstan shows greater wettability due to its native oxide layer, which lowers the effective surface tension and allows partial spreading. Upon addition of NaOH solution, the oxide layer is chemically removed, revealing the intrinsic high-tension metal interface and significantly reducing wettability, causing the droplets to contract into near-spherical shapes.

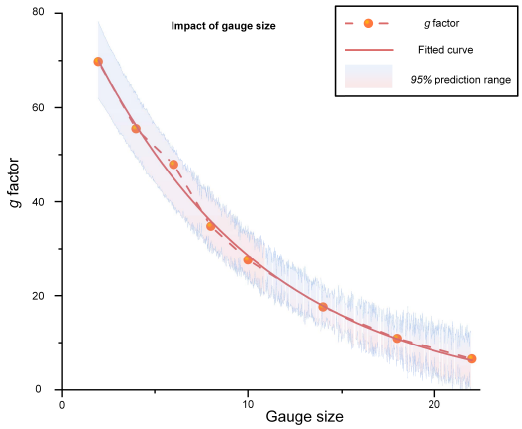

Supplementary Fig. 4 — g factor with different gauge size.

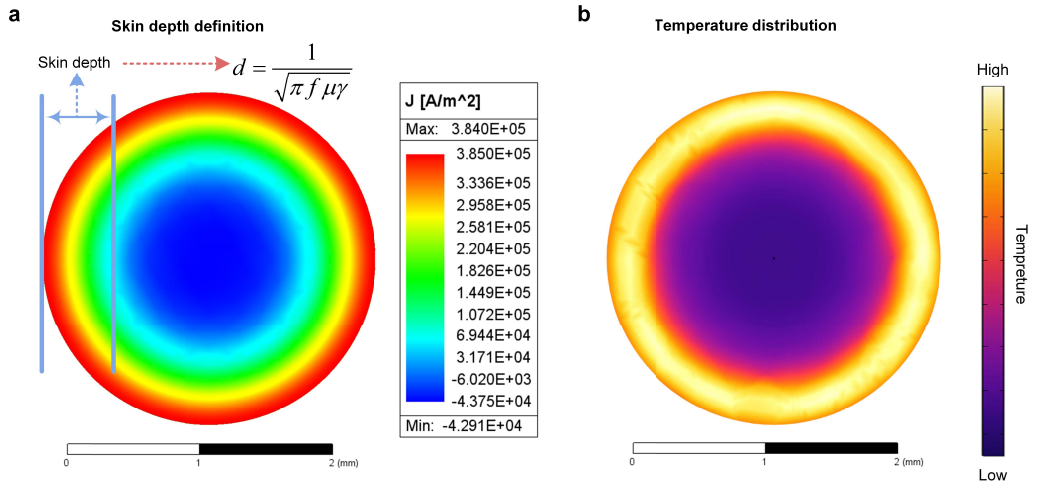

Supplementary Fig. 5 — Simulation diagram of current density and heat distribution in traditional conductors at high frequencies. a, Definition of skin depth of a cylindrical conductor at 20kHz. b, Temperature distribution of a cylindrical conductor at high frequency.

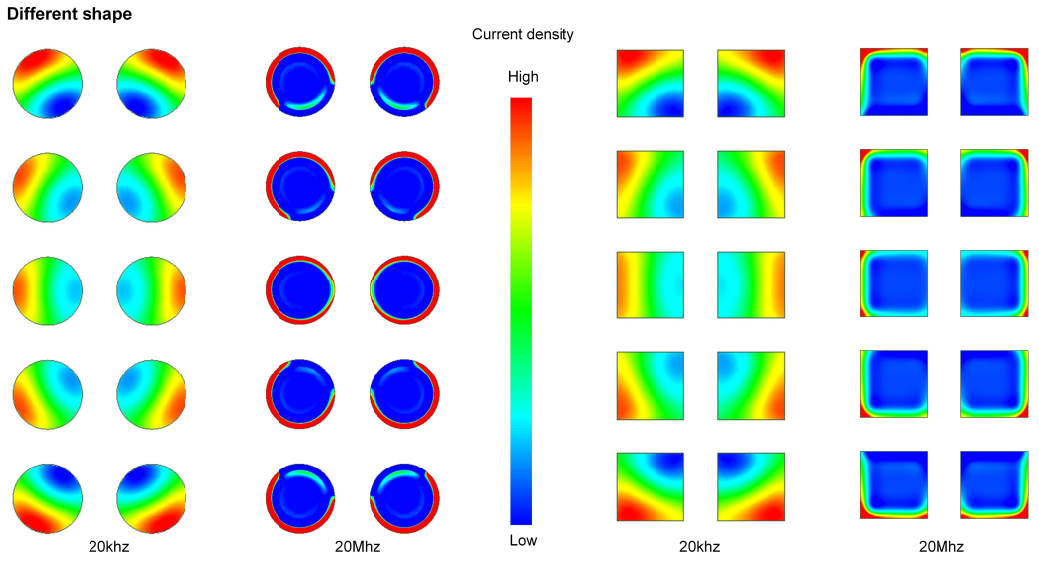

Supplementary Fig. 6 — Current density distribution in the cylindrical and rectangular windings of the transformer at 20 kHz and 20 MHz[7].

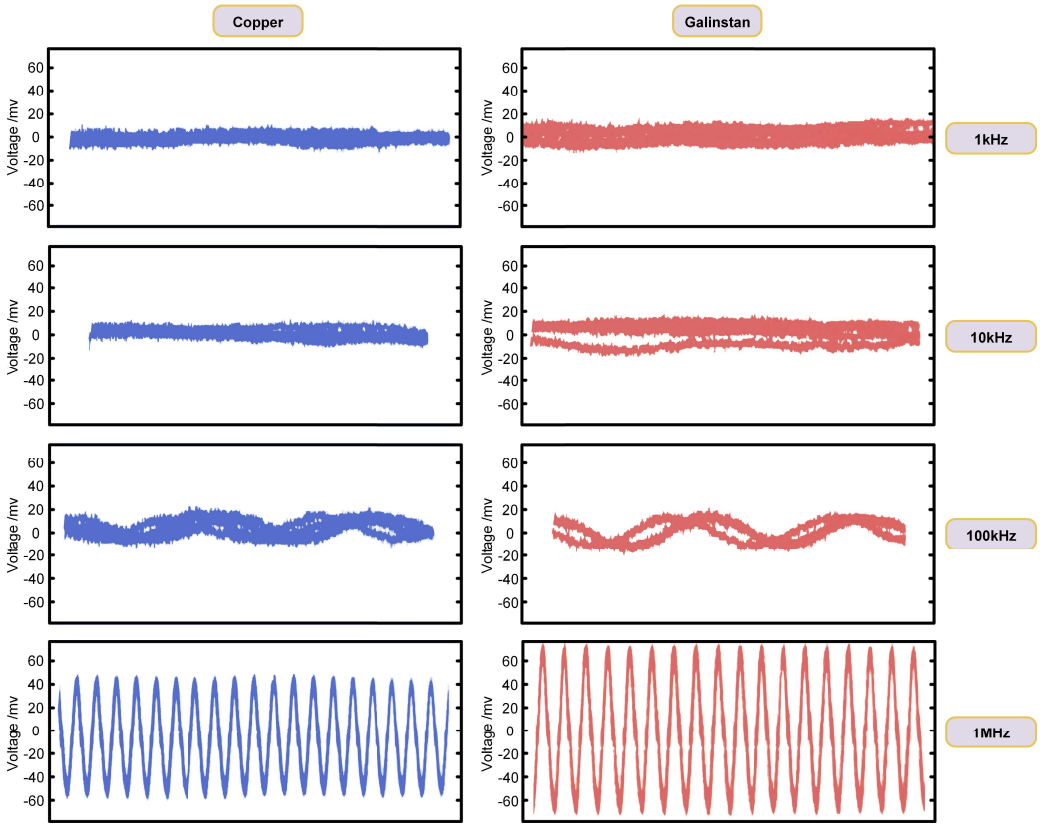

Supplementary Fig. 7 — Voltage drop comparison between Galinstan and a copper conductor of identical size at different frequencies. Voltage drop comparison between Galinstan and a copper conductor of identical size at different frequencies.

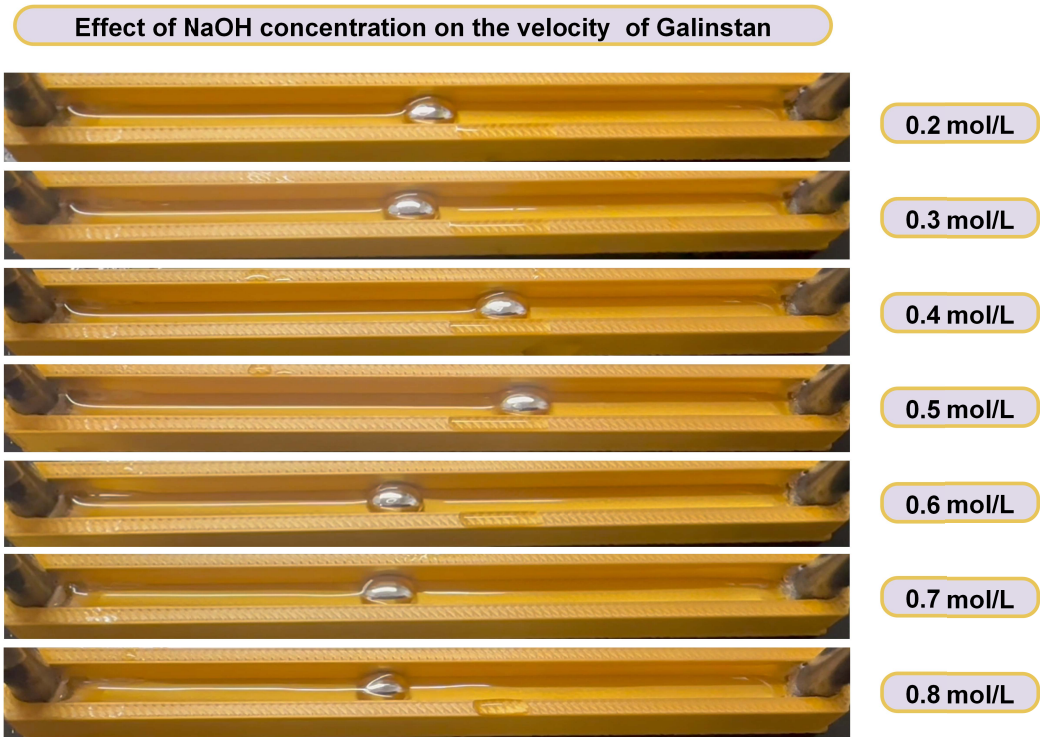

Supplementary Fig. 8 — Five experiments investigating the influence of various factors on LMC motion. Five experiments investigating the influence of various factors on LMC motion.

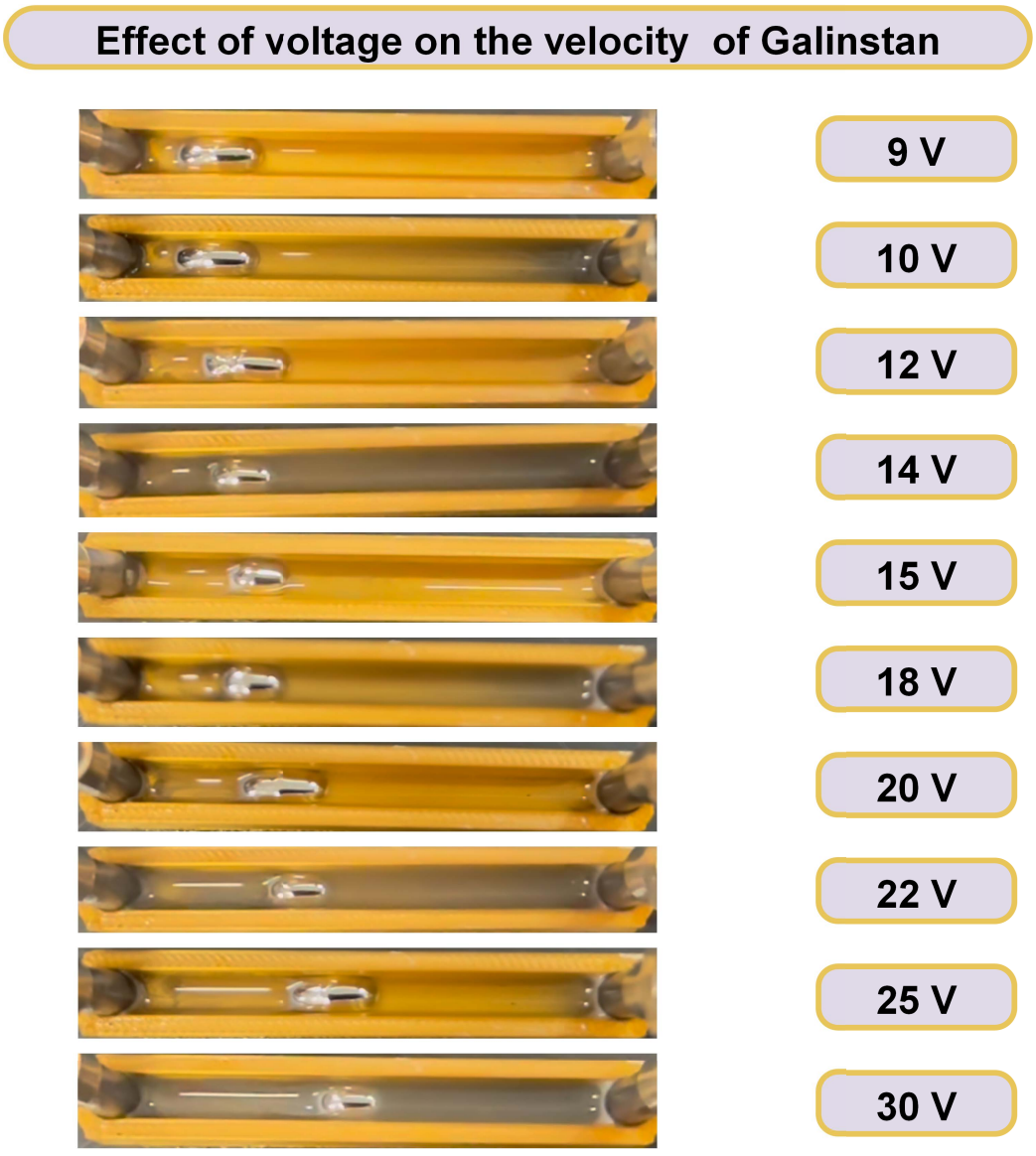

Supplementary Fig. 9 — Five experiments investigating the influence of various factors on LMC motion. Five experiments investigating the influence of various factors on LMC motion.

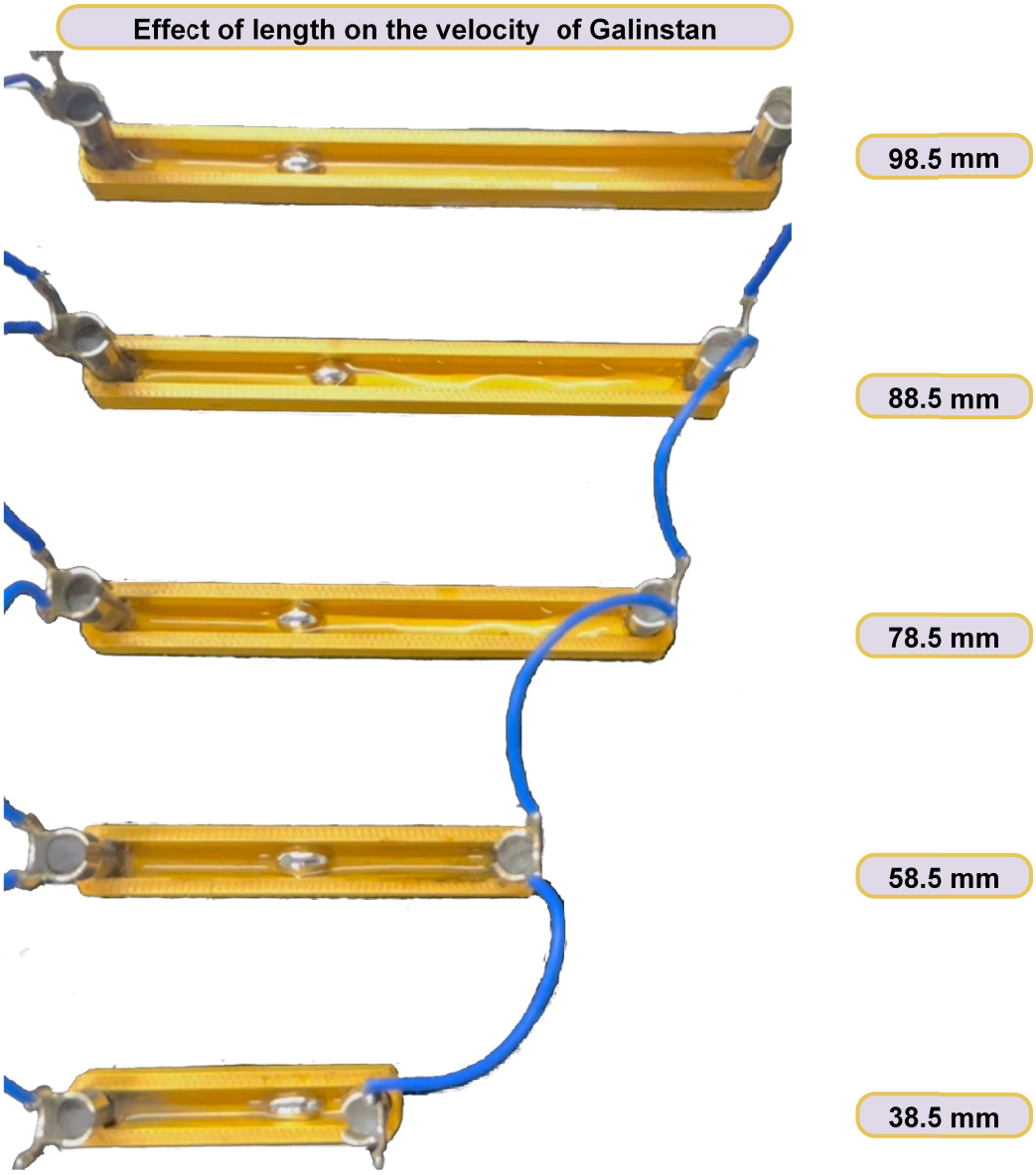

Supplementary Fig. 10 — Five experiments investigating the influence of various factors on LMC motion. Five experiments investigating the influence of various factors on LMC motion.

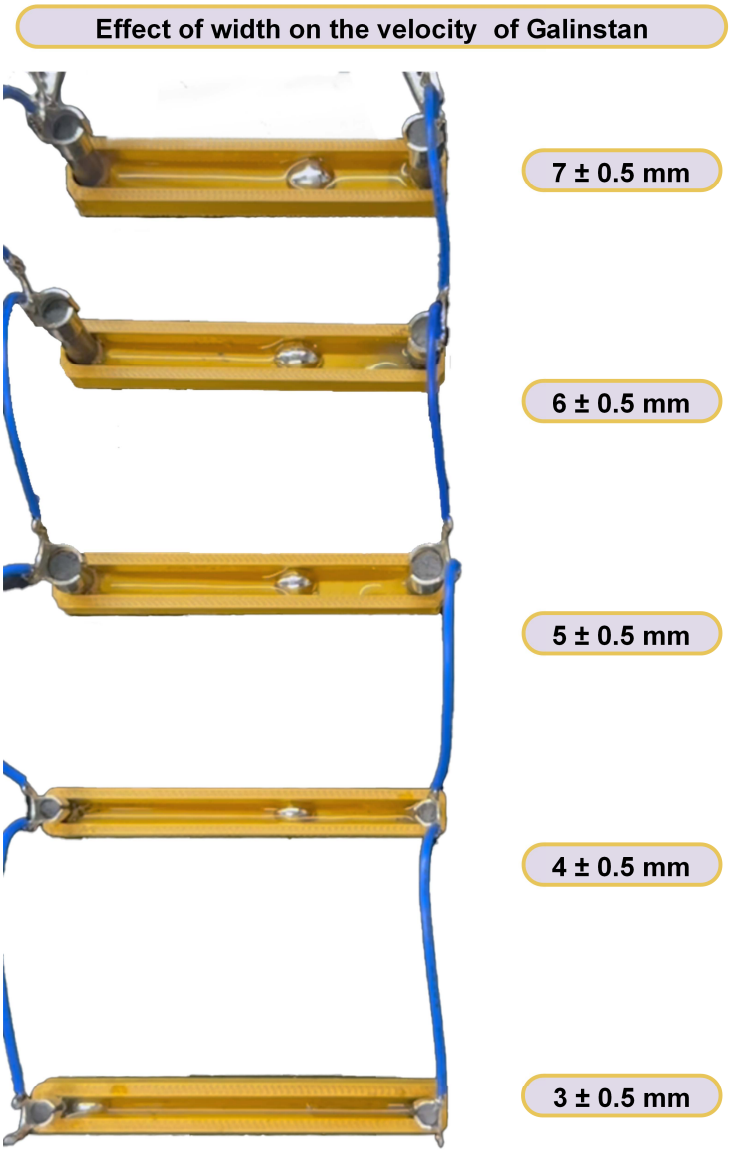

Supplementary Fig. 11 — Five experiments investigating the influence of various factors on LMC motion. Five experiments investigating the influence of various factors on LMC motion.

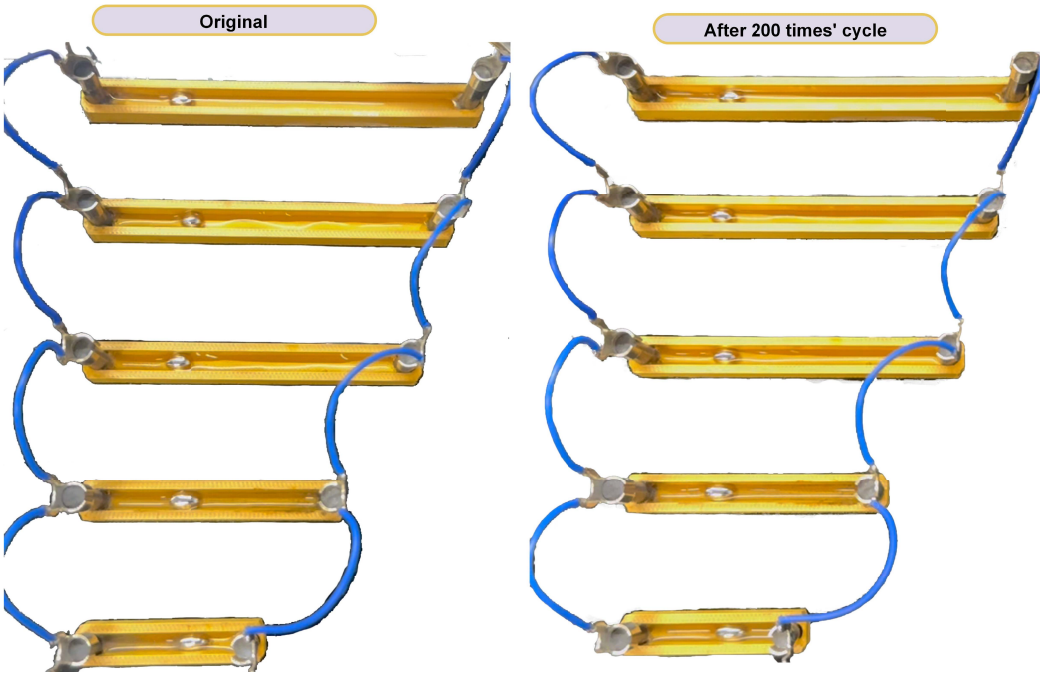

Supplementary Fig. 12 — Five experiments investigating the influence of various factors on LMC motion. Five experiments investigating the influence of various factors on LMC motion.

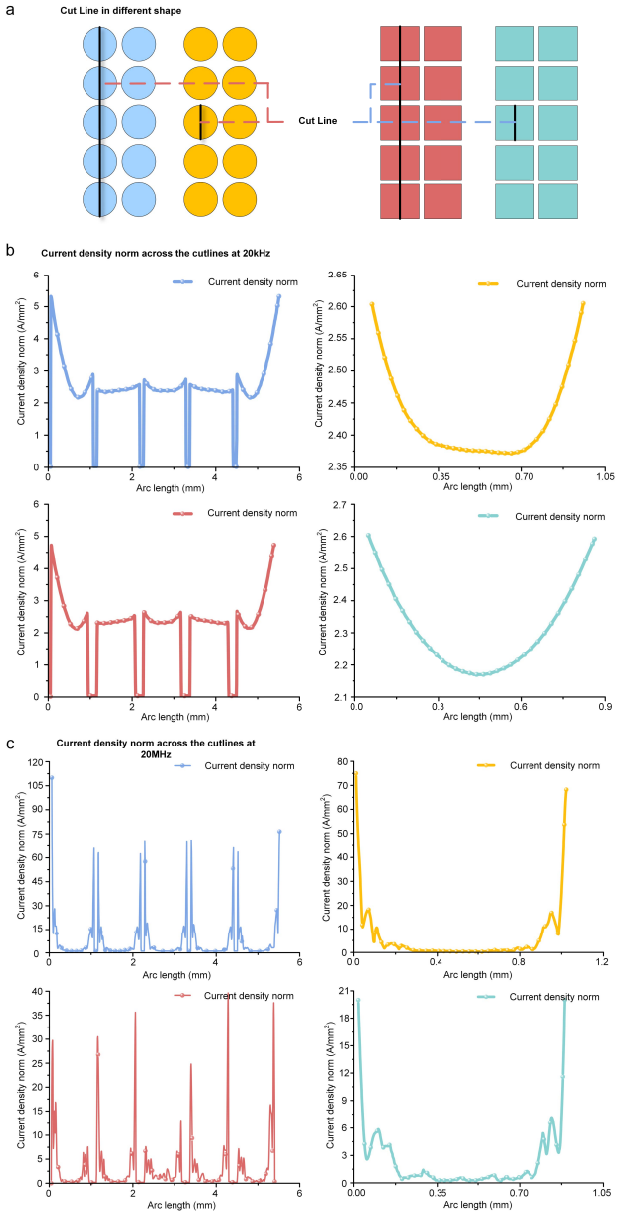

Supplementary Fig. 13 — Results of Current density at different frequency in a different shape High-Frequency DC-DC converter. a, Defined cutline across the cylindrical and rectangular conductors (Colors correspond to images) b, Current density norm (A/mm2) across the defined cutline in a from bottom to above at 20 kHz[6] c, Current density norm (A/mm2) across the defined cutline in a from bottom to above at 20 MHz[7].

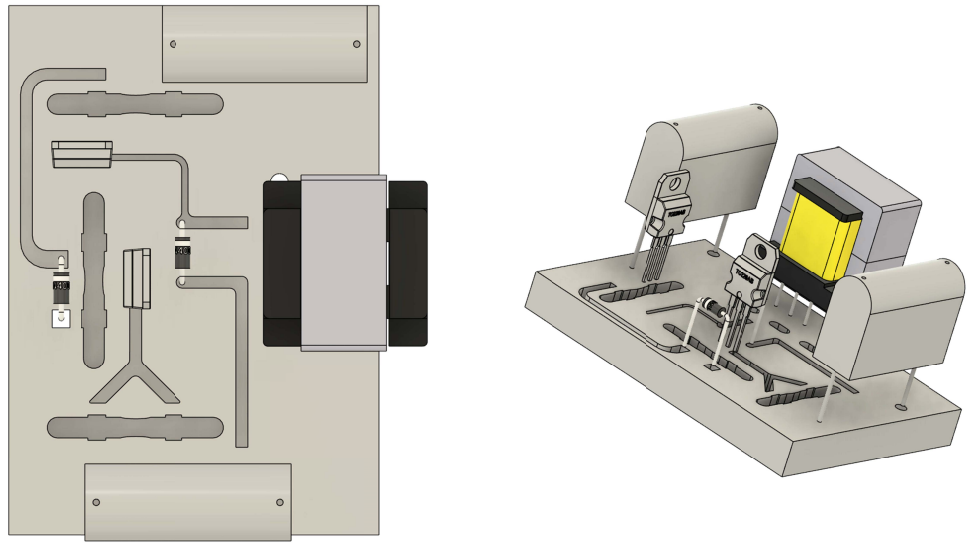

Supplementary Fig. 14 — Original flyback to half-bridge model diagram with top and side views, including main components and base plate

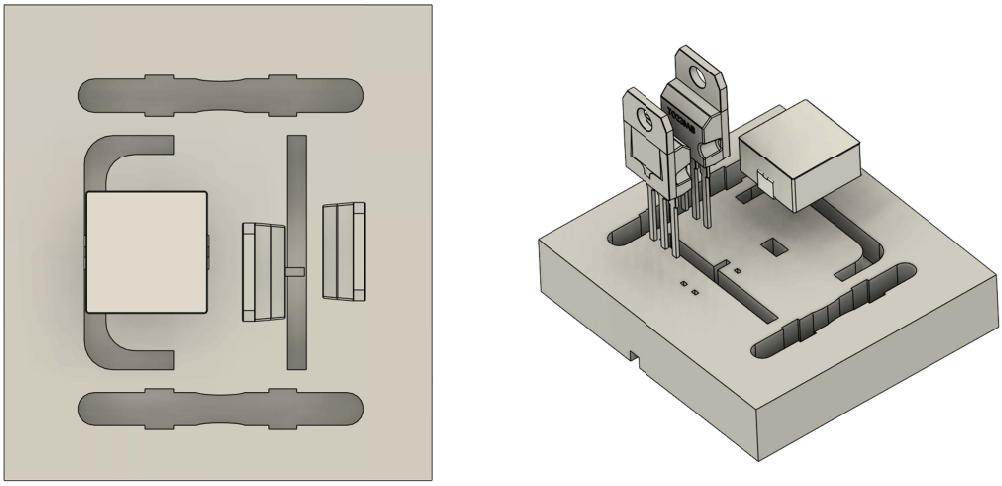

Supplementary Fig. 15 — Original buck to boost model diagram with top and side views, including main components and base plate

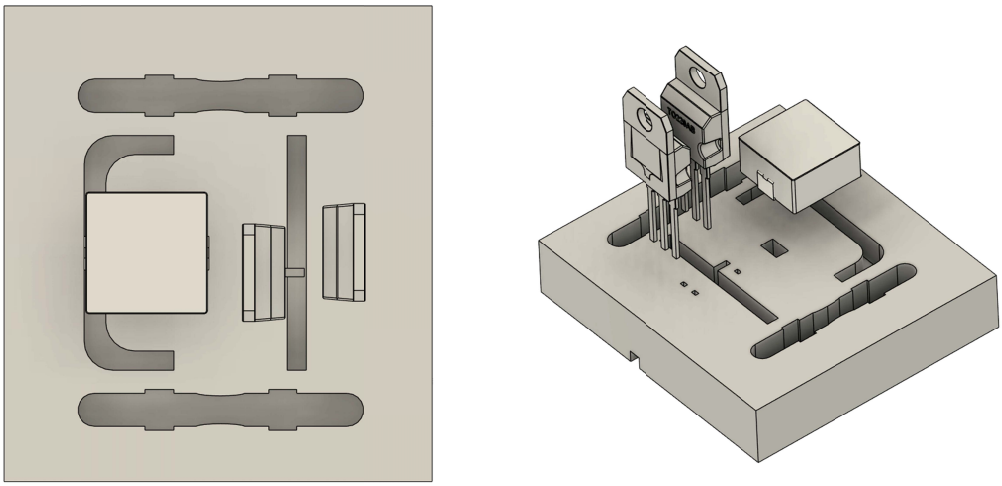

Supplementary Fig. 16 — Photo of controller and gate driver circuit

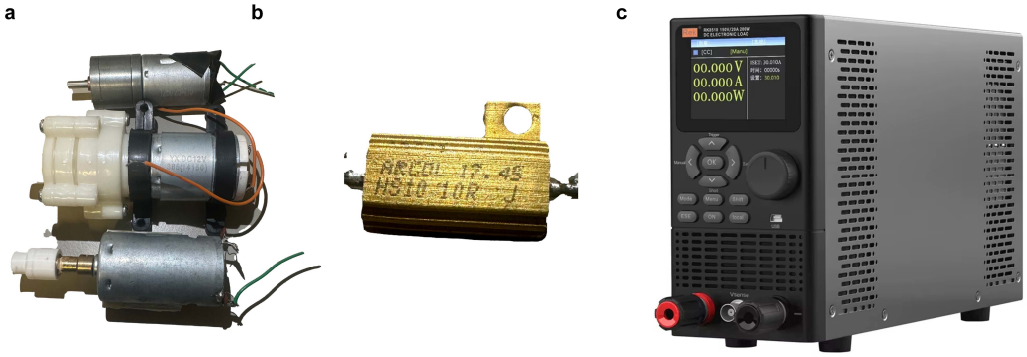

Supplementary Fig. 17 — Load type for the LHPC Buck circuit a, Inductive load composed of three motors connected in parallel. b, Resistive load composed of three parallel resistors. c, DC electronic load (RK8510B 500V/15A 400W) used for heavy-load testing.

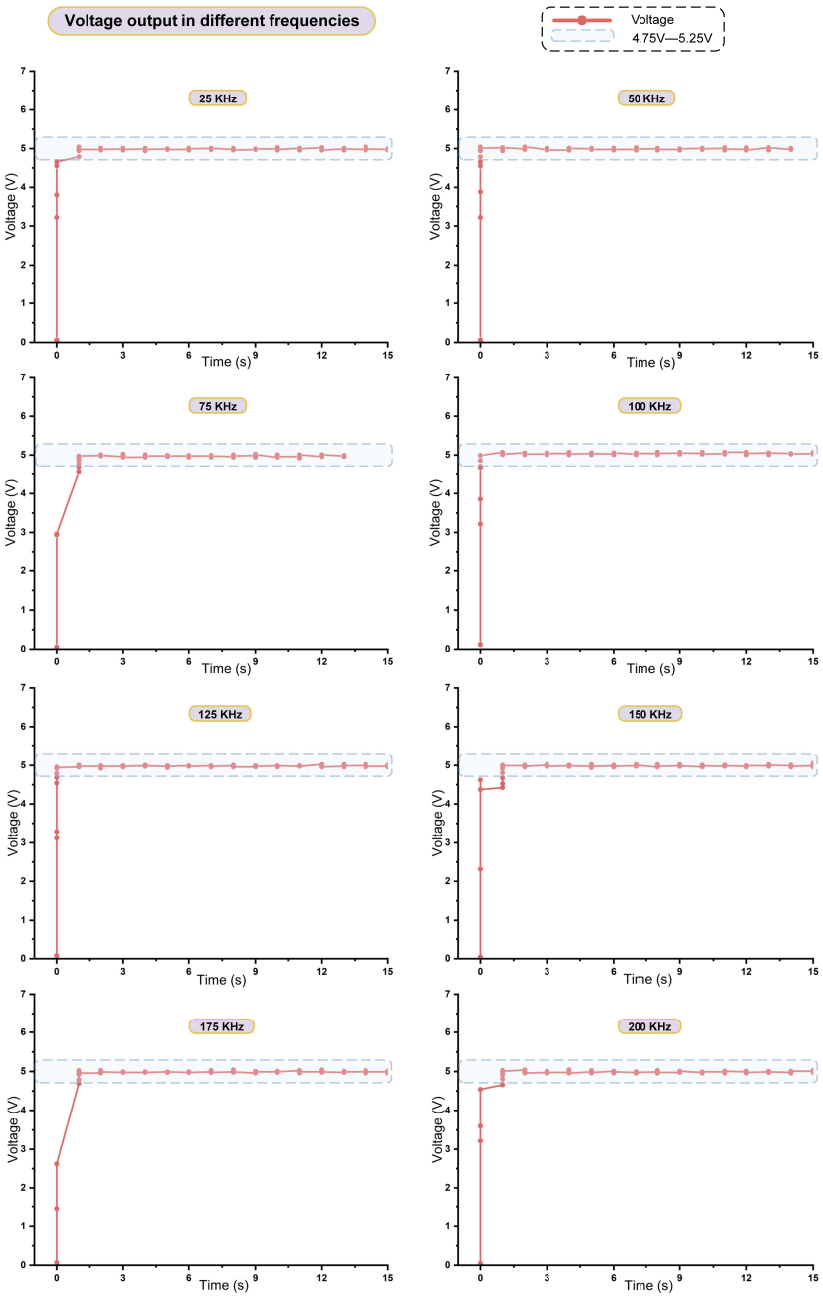

Supplementary Fig. 18 — Voltage output without load at different frequencies for the LHPC Buck circuit

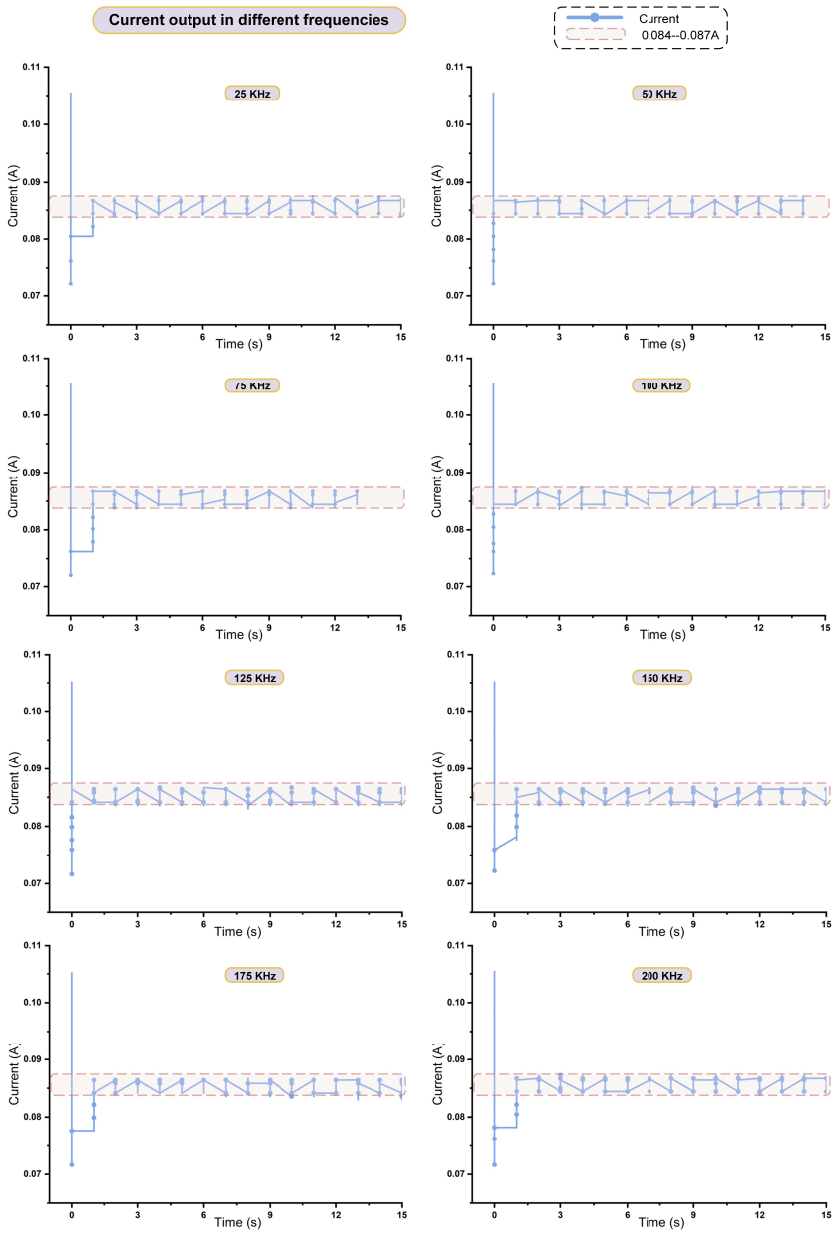

Supplementary Fig. 19 — Current output without load at different frequencies for the LHPC Buck circuit

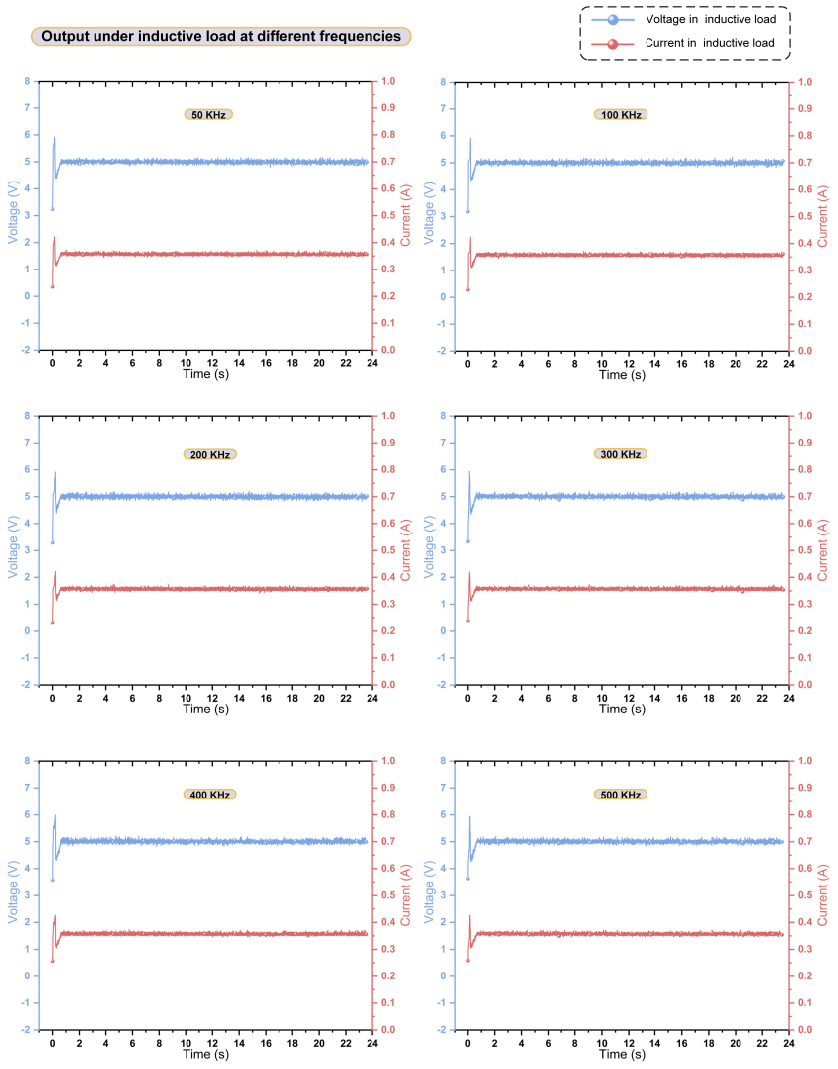

Supplementary Fig. 20 — Output under inductive load at different frequencies for the LHPC Buck circuit

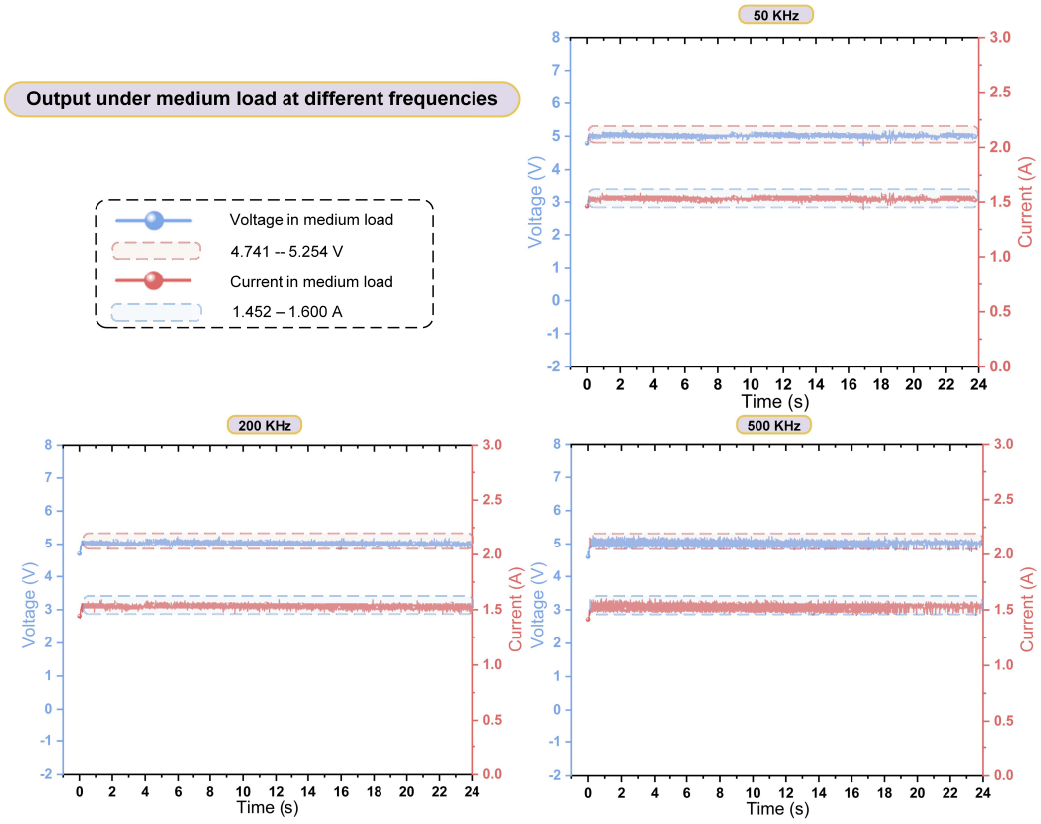

Supplementary Fig. 21 — Output under medium resistive load at different frequencies for the LHPC Buck circuit

Supplementary Tables

Supplementary Table 1a — Physical properties of various liquid metals and water.

Material	**MP (°C)**	**Vapor pressure (Pa)**	**Surface tension ($\mathbf{N\,m^{-1}}$)**
Mercury	38.8	1 (42°C)	487×10^{-3}
Gallium	29.8	$\approx 10^{-35}$ (29.9°C)	707×10^{-3}
NaK	-12.6	0.1 (25°C)	0.19
Rubidium	38.9	1.56×10^{-4} (39.5°C)	N/A
Cesium	28.4	N/A	N/A
EGaIn ($Ga_{75.5}In_{24.5}$)	15.5	N/A	624×10^{-3}
Galinstan ($Ga_{68.5}In_{21.5}Sn_{10}$)	-19	1.33×10^{-6} (500°C)	718×10^{-3}
Field's metal ($Bi_{32.5}In_{51}Sn_{16.5}$)	62	N/A	N/A
Wood's metal ($Bi_{41.5}Pb_{20.5}Sn_{13.3}Cd_{19.8}$)	70	N/A	N/A
Water	0	3169 (25°C)	72×10^{-3}

Supplementary Table 1b — Physical properties of various liquid metals and water.

Material	**Viscosity (Pa s)**	**Conductivity ($\mathbf{S\,m^{-1}}$)**	**Thermal cond. ($\mathbf{W\,m^{-1}\,K^{-1}}$)**	**Density ($\mathbf{g\,cm^{-3}}$)**
Mercury	1.53×10^{-3}	1.04×10^{6}	8.5	13.55
Gallium	1.37×10^{-3}	6.73×10^{6}	29.3	6.09
NaK	4.3×10^{-4}	3.3×10^{6}	22	0.855
Rubidium	N/A	7.79×10^{6}	58.2	1.532
Cesium	N/A	N/A	N/A	1.8785
EGaIn ($Ga_{75.5}In_{24.5}$)	1.99×10^{-3}	3.40×10^{6}	26.6	6.28
Galinstan ($Ga_{68.5}In_{21.5}Sn_{10}$)	2.40×10^{-3}	3.46×10^{6}	16.5	6.44
Field's metal ($Bi_{32.5}In_{51}Sn_{16.5}$)	N/A	N/A	N/A	N/A
Wood's metal ($Bi_{41.5}Pb_{20.5}Sn_{13.3}Cd_{19.8}$)	N/A	N/A	N/A	N/A
Water	1×10^{-3}	$< 5 \times 10^{-4}$	0.6	0.998

Supplementary Movies

Supplementary Movie 1. Actual experiment process video: Flyback to Half-bridge converter reconfiguration.
Supplementary Movie 2. Actual experiment process video: Half-bridge to Flyback converter reconfiguration.
Supplementary Movie 3. Actual experiment process video: bidirectional reconfiguration between Buck and Boost converters.

References

[1] Beni, G., Hackwood, S. & Jackel, J. L. Continuous electrowetting effect. *Applied Physics Letters* **40**, 912–914 (1982).

[2] Wang, M., Jin, M., Jin, X. & Zuo, S. Modeling of movement of liquid metal droplets driven by an electric field. *Physical Chemistry Chemical Physics* **19**, 18505–18513 (2017).

[3] Song, C.-L. *et al.* Fluid pumping by liquid metal droplet utilizing ac electric field. *Physical Review E* **105**, 025102 (2022).

[4] Li, X. *et al.* Kinetic drop friction. *Nature communications* **14**, 4571 (2023).

[5] Chen, Y. *et al.* Robust fabrication of nonstick, noncorrosive, conductive graphene-coated liquid metal droplets for droplet-based, floating electrodes. *Advanced Functional Materials* **28**, 1706277 (2018).

[6] Hayt, W. H. & Buck, J. A. *Engineering Electromagnetics* 8 edn (McGraw-Hill, New York, NY, 2012).

[7] Nia, M. S. S., Saadatmand, S., Altimania, M., Shamsi, P. & Ferdowsi, M. Analysis of skin effect in high frequency isolation transformers. *Proc. North American Power Symposium (NAPS)*, 1–6 (2019).

[8] Terman, F. E. *Radio Engineers' Handbook* (McGraw-Hill, New York, 1943).

[9] Ferreira, J. A. Appropriate modelling of conductive losses in the design of magnetic components. *Proceedings of the 21st Annual IEEE Power Electronics Specialists Conference (PESC)*, 780–785 (1990).

[10] Ferreira, J. A. Improved analytical modeling of conductive losses in magnetic components. *IEEE transactions on Power Electronics* **9**, 127–131 (1994).

[11] Dowell, P. Effects of eddy currents in transformer windings. *Proceedings of the Institution of electrical Engineers* **113**, 1387–1394 (1966).

[12] Solomentsev, M. & Hanson, A. J. Modeling current distribution within conductors and between parallel conductors in high-frequency magnetics. *IEEE Open Journal of Power Electronics* **3**, 635–650 (2022).

[13] Sheng, Y. *et al.* Application of high-density electropulsing to improve the performance of metallic materials: Mechanisms, microstructure and properties. *Materials* **11**, 185 (2018).

[14] Rossmanith, H., Doebroenti, M., Albach, M. & Exner, D. Measurement and characterization of high frequency losses in nonideal litz wires. *IEEE Transactions on Power Electronics* **26**, 3386–3394 (2011).

[15] Al Eit, M., Bouillault, F., Marchand, C. & Krebs, G. 2-d reduced model for eddy currents calculation in litz wire and its application for switched reluctance machine. *IEEE Transactions on Magnetics* **52**, 1–4 (2015).